ACS APPLIED MATERIALS & INTERFACES

Research Article

Cite This: ACS Appl. Mater. Interfaces 2020, 12, 3494−3501

www.acsami.org

Scalable Freeze-Tape-Casting Fabrication and Pore Structure Analysis of 3D LLZO Solid-State Electrolytes

Hao Shen,[†,‡] Eongyu Yi,[‡] Stephen Heywood,[∥] Dilworth Y. Parkinson,[§] Guoying Chen,[‡] Nobumichi Tamura,[§] Stephen Sofie,[∥] Kai Chen,[*,†] and Marca M. Doeff[*,‡]

[†]Center for Advancing Materials Performance from the Nanoscale (CAMP-Nano), State Key Laboratory for Mechanical Behavior of Materials, Xi'an Jiaotong University, Xi'an, Shaanxi 710049, China

[‡]Energy Storage and Distributed Resources Division and [§]Advanced Light Source, Lawrence Berkeley National Laboratory, Berkeley, California 94720, United States

[∥]Department of Mechanical & Industrial Engineering, Montana State University, Bozeman, Montana 59715, United States

Supporting Information

ABSTRACT: Nonflammable solid-state electrolytes can potentially address the reliability and energy density limitations of lithium-ion batteries. Garnet-structured oxides such as $Li_7La_3Zr_2O_{12}$ (LLZO) are some of the most promising candidates for solid-state devices. Here, three-dimensional (3D) solid-state LLZO frameworks with low tortuosity pore channels are proposed as scaffolds, into which active materials and other components can be infiltrated to make composite electrodes for solid-state batteries. To make the scaffolds, we employed aqueous freeze tape casting (FTC), a scalable and environmentally friendly method to produce porous LLZO structures. Using synchrotron radiation hard X-ray microcomputed tomography, we confirmed that LLZO films with porosities of up to 75% were successfully fabricated from slurries with a relatively wide concentration range. The acicular pore size and shape at different depths of scaffolds were quantified by fitting the pore shapes with ellipses, determining the long and short axes and their ratios, and investigating the equivalent diameter distribution. The results show that relatively homogeneous pore sizes and shapes were sustained over a long range along the thickness of the scaffold. Additionally, these pores had low tortuosity and the wall thickness distributions were found to be highly homogeneous. These are desirable characteristics for 3D solid electrolytes for composite electrodes, in terms of both the ease of active material infiltration and also minimization of Li diffusion distances in electrodes. The advantages of the FTC scaffolds are demonstrated by the improved conductivity of LLZO scaffolds infiltrated with poly(ethylene oxide)/lithium bis(trifluoromethanesulfonyl)imide (PEO/LITFSI) compared to those of PEO/LiTFSI films alone or composites containing LLZO particles.

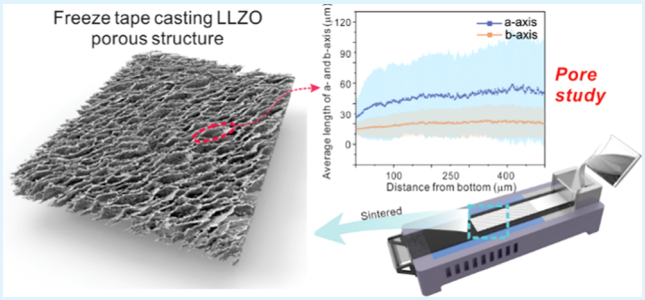

KEYWORDS: *solid-state electrolyte, freeze tape casting (FTC), hard X-ray microcomputed tomography, structure analysis, LLZO*

INTRODUCTION

Solid-state batteries have great potential to improve energy density and safety over what is currently achievable with lithium-ion batteries (LIBs). The absence of flammable liquid electrolytic solutions reduces the risk of fire and leakage and also may allow reliable cycling of lithium metal anodes. Replacing the graphite anode in LIBs with metallic lithium can result in much higher energy density and specific energy due to the 10-fold higher specific capacity (3860 mAh/g) of the latter.[1,2] In conventional batteries with liquid electrolytic solutions, repeated cycling of lithium metal anodes can lead to dendritic shorting or mossy deposition, which are significant factors in their catastrophic failures.[3] Another advantage of solid-state devices is the possibility of using bipolar designs,[4−6] which can further save weight and space. The superior characteristics of garnets related to $Li_7La_3Zr_2O_{12}$ (LLZO) include a wide voltage stability window of nearly 6 V, good thermal stability, high ionic conductivity (~0.1−1.3 mS/cm), and excellent mechanical properties, making them among the most promising of the solid electrolyte systems.[5,7−12] There were early reports of high interfacial impedances between lithium metal and LLZO but these have largely been overcome by modifying interfaces and electrode designs, and stable cycling can now be reliably achieved in symmetrical cells at current densities of up to 10 mA/cm^2.[13−16] To fully realize the promise of these devices, however, innovations in the design and fabrication of cathodes are now required. Most commercial solid-state batteries employ thin film formats, in which the areal capacities of the electrodes are very low, resulting in energy densities that are only a small fraction of the

Received: July 5, 2019
Accepted: December 20, 2019
Published: December 20, 2019

DOI: 10.1021/acsami.9b11780
ACS Appl. Mater. Interfaces 2020, 12, 3494−3501

theoretical values and limiting applications. Thicker electrodes, similar to what are used in LIBs (30−100 μm), would result in higher practical energy densities, as well as require that the active material be composited with the ionic conductor and other additives to overcome transport limitations. Furthermore, all solid-state formats present formidable engineering challenges associated with establishing and maintaining intimate contact among the components during cycling.[17,18] Some attempts have already been made to create three-dimensional (3D) LLZO frameworks for composite electrode structures through the use of fiber templating during tape casting[17] and 3D printing.[18] The thickness of the composite electrode was well controlled to be around 100 μm. Fiber templating creates a high tortuosity porous structure but is suitable for infiltrating molten sulfur. Proof-of-principle studies have been carried out for these composite electrodes. As claimed, the total energy density (248 W h kg^{-1}) is far beyond that of any solid battery today.

Freeze tape casting (FTC) is a scalable method to produce highly porous ceramic structures with easily controllable pore architectures. When water is used, it is also an environmentally friendly process. The technique has been successfully applied to produce porous Y:ZrO_2 (YSZ) scaffolds for solid oxide fuel cells, to improve fuel gas inflow, and to increase the contact area among components by generating large homogeneously distributed pores inside a ceramic body.[19−21] Here, we demonstrate using FTC to prepare LLZO scaffolds for solid-state battery applications, which can be infiltrated with active material and electronically conductive additives to make composite cathodes,[12] or with polymer electrolytes to make composite ion-conducting layers. To this end, we prepared several scaffolds using different solid loadings in the slurries. Combined with the detailed examination of the pore structures, we aim to understand how processing parameters affect the porosity and how this critical design can influence the performance of electrodes and composite electrolytes. To do the latter, we used the high penetration depth and spatial resolution of high-energy synchrotron radiation hard X-ray microcomputed tomography (SR-μCT)[22] to reconstruct three-dimensional (3D) models of the FTC LLZO structures. The 3D morphology study using SR-μCT is meant to establish better knowledge about the feasibility of freeze tape casting as applied to solid-state battery fabrication. The ultimate goal of this work is to obtain information pertinent to the optimization of composite cathodes or solid electrolyte layers based on FTC structures for use in solid-state batteries.

EXPERIMENTAL SECTION

LLZO powder (Ampcera, Al-doped $Li_{6.25}Al_{0.25}La_3Zr_2O_{12}$, MSE) was used as received and mixed with up to 20 wt % Li_2CO_3 (Alfa Aesar) that served as both sintering aid and source of excess lithium to promote the cubic garnet (c-LLZO) structure during high-temperature sintering. The combined powders were mixed in an aqueous suspension at solid loadings of 7.5, 12.5, and 17.5 vol %, utilizing an ammonium polymethacrylate salt dispersant (Darvan C−N, Vanderbilt Minerals, LLC) at 2 wt % of the solid content. Although water induces slow decomposition of LLZO[23,24] resulting in protonation and formation of Li_2CO_3, the addition of excess Li from Li_2CO_3 added to the slurry and subsequent heating reverse the process as has been described in our previous studies.[25,26] At such low solid loading, the slurry has insufficient viscosity to prevent dewetting on the Mylar tape-casting carrier film and to maintain a doctor blade gap height after casting; therefore, 0.3 wt % (of the water content) xanthan gum (Vanzan D, Vanderbilt Minerals, LLC) was incorporated as a thickener. The resulting mixture was ball-milled in polyethylene bottles with Al_2O_3 milling media for 24 hrs to properly homogenize the precursor powders and the thickener to achieve a stable slurry. An acrylic emulsion binder (Rhoplex HA-12, 53 wt % polymeric solid emulsion, Dow Chemical) was utilized to provide strength to the high-porosity LLZO scaffolds, and the water emulsion binder was mixed with the LLZO suspension at 35 wt % of the ceramic solid content. Prior to casting, the slurry was deaired under a ~10^{-3} mbar vacuum with the addition of a defoamer (Surfynol PC Defoamer, Evonik) to release trapped air in the slurry.

The homemade freeze-tape-casting setup is shown in Figure 1. Slurries with various LLZO solid loadings were poured through a

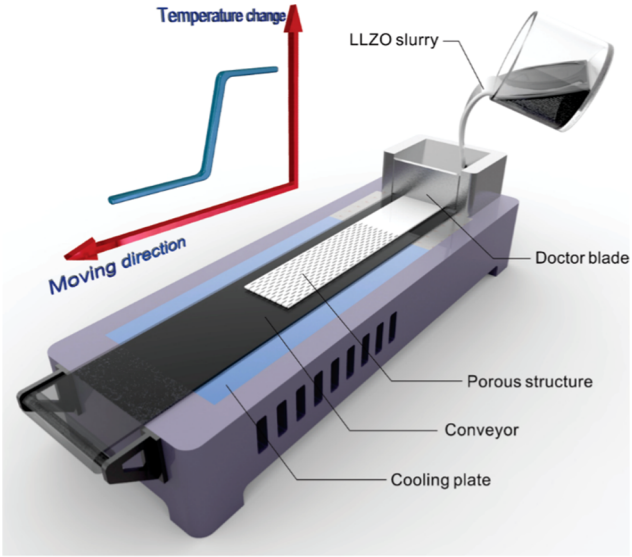

Figure 1. Schematic of the freeze-tape-casting setup.

sieve drainer to remove any agglomerates into the reservoir, and cast onto the silicone-coated Mylar film that was carried out by the conveyor belt at a constant speed of 0.5 mm/s to maintain a uniform solidification front on the freezing bed, which was set at −40 °C for this study. Slurries with three different loadings (7.5, 12.5, and 17.5%) of LLZO were utilized, and the LLZO tape thickness in all cases was set to be about 630 μm by the use of a doctor blade. After freeze drying overnight at −50 °C to sublimate the solvent crystals, the LLZO porous tapes were first punched into regular cylindrical pieces and sintered at 1000 °C for 2 h in an Ar gas on Grafoil substrates to prevent sample sticking during densification. To ensure the best SR-μCT contrast, the freeze-tape-cast LLZO samples were encapsulated in epoxy and then cut into cylinders with a diameter of 3 mm, oriented along the thickness of the LLZO film.

The SR-μCT characterization was performed at beamline 8.3.2 of the Advanced Light Source (ALS) at Lawrence Berkeley National Laboratory. First, several bright- and dark-field images were collected to correct the X-ray beam intensity fluctuation and normalize the background. Bright-field images were recorded with an X-ray beam exposure but without the sample in the field of view (FOV), whereas dark-field images were acquired for detector background without the illumination of an X-ray beam. During the experiment, the cylindrical sample was mounted on a rotational stage with the sample thickness axis vertical and centered in the FOV. The sample was rotated at 0.125° incremental steps for a total of 180°. At each step, the sample was exposed with a monochromatic 24 keV X-ray beam for 0.5 s. The transmitted X-ray beam was recorded using a 50 μm thick LuAG:Ce scintillator, a 10× Olympus objective lens, and a PCO.edge sCMOS detector. Each raw projection represents a two-dimensional X-ray attenuation map, which was used to reconstruct a 3D data volume. Xi-CAM[27] and TomoPy[28] were employed to reconstruct the 3D models, while the visualization and subvolume selection were done by Avizo from FEI. The frame-by-frame analysis was carried out using

DOI: 10.1021/acsami.9b11780
ACS Appl. Mater. Interfaces 2020, 12, 3494−3501

ImageJ.[29] For each specimen, two subvolumes were selected for detailed study. One was a thin film shaped with the volume of interest of 1046 × 1403 × 128 μm^3, with the thickness direction of the subvolume parallel to the thickness axis of the cast LLZO tape. For a better comparison, the thin-film-shaped subvolume of each specimen was chosen from almost exactly the middle of each specimen along the freezing direction, and the thickness of 128 μm was selected because this is close to the thickness of the electrodes commonly used in cells. The other subvolume was a longitudinal section with a square (128 × 128 μm^2) cross section and a long axis of 631 μm parallel to the LLZO tape thickness to investigate the channel morphology and wall thickness evolution along the freezing direction. Note that the thicknesses of the subvolumes are larger than those of the samples to ensure imaging of the top and bottom surfaces.

To quantify the size and morphology, the pores were fitted using ellipses. The experimentally collected tomographic image of the pores (Figure 2a as an example) was first Gaussian-smoothed and binarized

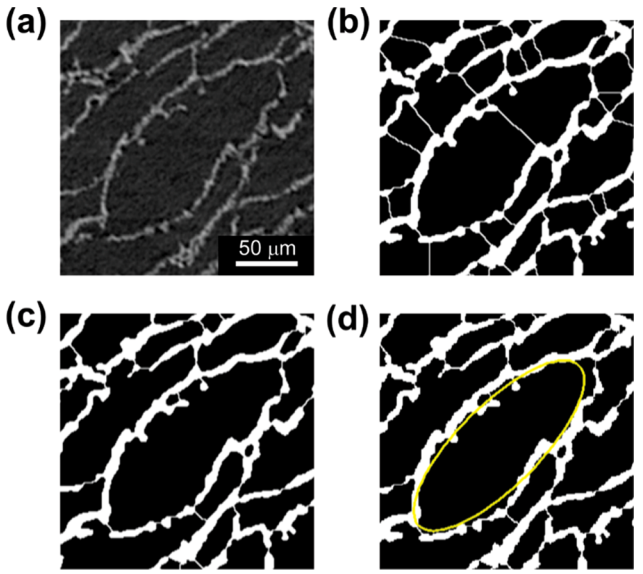

Figure 2. Data processing and ellipse fitting of pores. (a) Gaussian-smoothed and binarized tomographic image of the pores. The dark parts are pores, while the white lines are LLZO walls. Comparison with the splitting result obtained through a standard watershed algorithm (b). Irregular watershed approach mitigates the over-splitting problem (c). After splitting, the selected pore is fitted with a yellow ellipse (d).

and then segmented following the standard watershed algorithm. However, false pore splitting and fragmentation were frequently observed, as displayed by the thin white curves in Figure 2b. It was evident that ellipse fitting conducted directly on such binarized figures resulted in misleading statistics of the pore size distribution by generating a large quantity of artificial pores with relatively small size. To reduce the oversplitting mainly caused by watershed separation, a custom-developed irregular watershed feature implanted in a BioVoxxel Toolbox[30] was employed. By adjusting the so-called erosion cycle number parameter, the pores are reasonably well separated, mitigating the effects due to the roughness and disconnection of the pore walls (Figure 2c as a comparison to Figure 2b, with more reliable evidence shown in Figure S1 in the Supporting Information (SI)). Finally, the size and shape of the segmented pores were determined by ellipse fitting, adopting the algorithm developed by Wagner and Eglinger,[31] as indicated by the yellow ellipse in Figure 2d.

For the composite electrolytes, PEO [poly(ethylene oxide), M_v = 900 k] and bis(trifluoromethane)sulfonimide lithium salt [LiTFSI] were dissolved in acetonitrile at a 20:1 ratio of EO/Li. The solution was cast onto a Teflon Petri dish and dried to form a polymer electrolyte film. LLZO powder/polymer composite electrolytes were also fabricated by introducing the LLZO powder into the polymer electrolyte solution, which was then ultrasonicated for 1 h prior to casting. LLZO scaffolds were infiltrated with the polymer electrolyte by repeatedly drop-casting the solution. The LLZO powder mass was selected to match the LLZO: polymer electrolyte ratio in the LLZO scaffold/polymer electrolyte counterpart (65:35 wt or 30:70 vol). All samples were dried under vacuum for several hours at 50 °C prior to measurements carried out at room temperature. Electrochemical impedance spectroscopy was measured using a Bio-Logic VMP3 potentiostat/galvanostat equipped with frequency response analyzers. Measurements were made in the frequency range of 300 kHz to 1 Hz.

RESULTS AND DISCUSSION

The 3D model and front view of the thin film subvolume, as well as the tomographic micrograph of the longitudinal section subvolume, of the freeze-tape-cast porous structures fabricated using slurries with various LLZO vol % are displayed in Figure 3. The porous structures made from low-concentration slurries (7.5 and 12.5%) are presented at selected viewing angles from the movies in the Supporting Information. From the 3D models and the front view cross sections in Figure 3a,b, it is obvious that unblocked and open pore channels are formed for both the 7.5 and 12.5% LLZO slurries. The slanting of the channels occurs because the temperature gradient is not perfectly aligned from bottom to top, as has also been reported previously.[21] The size of the channels is uniformly distributed in each sample, and higher LLZO concentrations result in decreased pore sizes. Quantitative measurement indicates that the porosities of these two specimens are 79% and 75%, respectively. An inspection of the longitudinal section subvolume indicates that there is roughly a constant LLZO wall thickness throughout the whole 630 μm cast tape thickness range, in contrast to the decreasing wall thickness from bottom to top in the yttria-stabilized zirconia (YSZ) sample fabricated using a similar freeze-tape-casting setup.[21] When the LLZO slurry concentration was raised to 17.5 vol %, however, the morphology of the LLZO structure changed dramatically (Figure 3c). Instead of aligned channels, randomly distributed holes, hundreds of microns in diameter, are generated. This structure is also displayed in a movie in the SI, together with a photograph for the whole cylinder (Figure S2, SI). Excessive powder/solvent interaction at higher LLZO vol % degraded the powder dispersion stability, which deterred uniform powder exclusion during ice nucleation and growth processes, and hence no ordered pore channels formed. This behavior was also observed in YSZ-based FTC, but at a substantially higher solid loading approaching 45 vol %, indicating that FTC methods for LLZO are ideal at high porosity, which coincides with the desired outcomes of LLZO composite cathode approaches.

The morphologies of the pores in the LLZO structures fabricated using 7.5 and 12.5 vol % slurries, labeled Sample 1 and Sample 2, respectively, throughout the manuscript, were analyzed in detail. The cross sections of both samples covering the whole thickness are displayed in Figure 4a,b. The longitudinal pore directions in both samples are not normal to the film surface but slanted, in contrast to other porous structures fabricated using the freeze-casting method.[32] More reconstructed models for displaying pores in the whole thickness direction are shown in Figures S3 and S4. Generally, larger pores and less connectivity (bridging) are apparent in Sample 1 compared to those in Sample 2, resulting from the higher solvent concentration.

DOI: 10.1021/acsami.9b11780
ACS Appl. Mater. Interfaces 2020, 12, 3494−3501

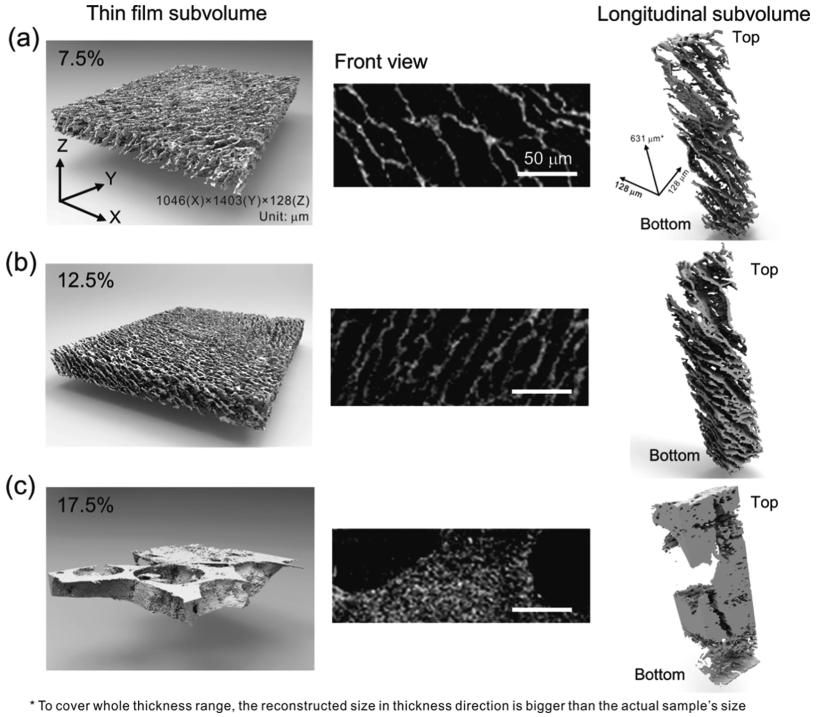

Figure 3. Reconstructed thin film and longitudinal subvolumes together with the front view images extracted from the tomographic results for the 7.5% (a), 12.5% (b), and 17.5% (c) structures, respectively.

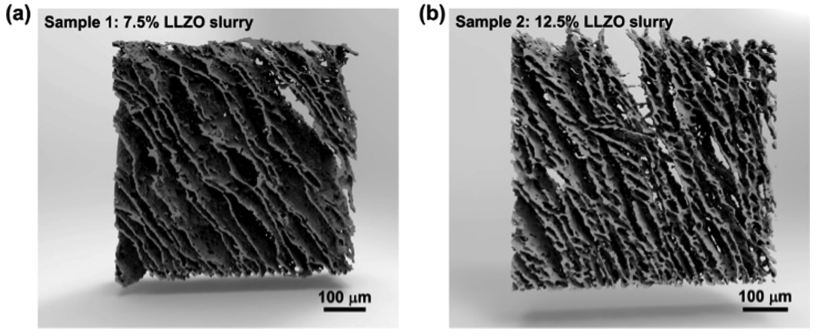

Figure 4. Morphology of the pores fabricated using 7.5% (a) and 12.5% (b) LLZO slurries.

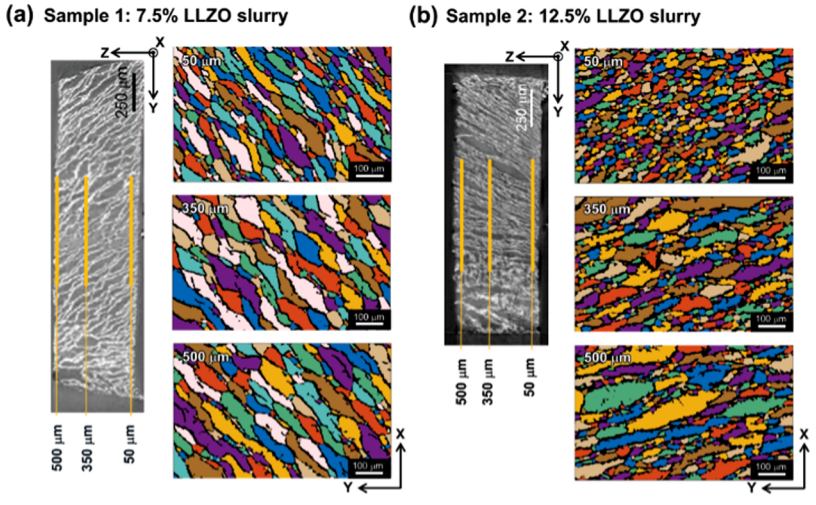

Figure 5. *XY* cross sections at various thickness positions in 7.5% (a) and 12.5% (b) samples. Pores are colored to distinguish from the surrounding ones. For both samples, the positions of the selected cross sections are labeled.

DOI: 10.1021/acsami.9b11780
ACS Appl. Mater. Interfaces 2020, 12, 3494−3501

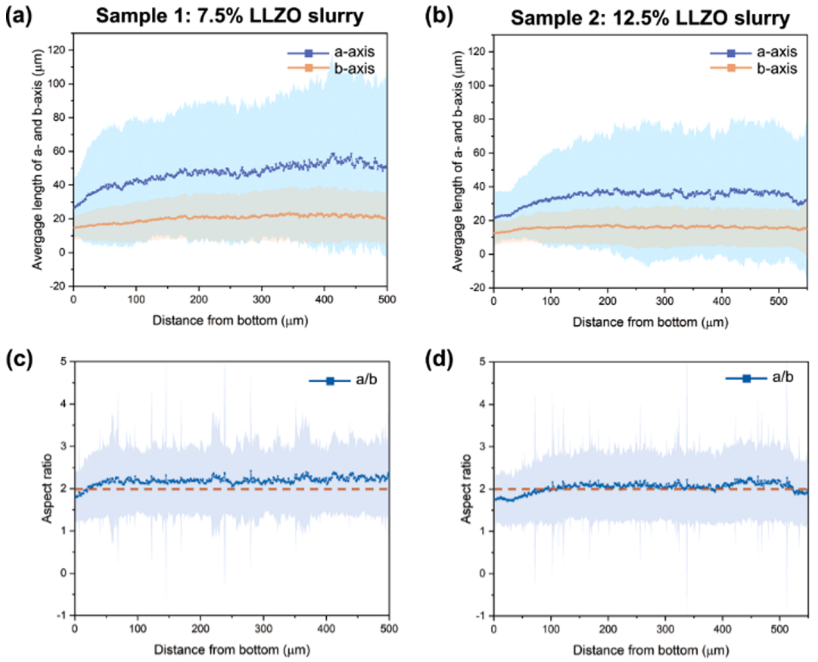

Figure 6. Lengths of long and short axes of pores averaged over each *XY* cross-sectional plane in 7.5% (a) and 12.5% (b) samples. The aspect ratios (c, d) are also calculated for both samples according to the measured long and short axes.

To better understand the pore morphology evolution along the film thickness (*Z*-direction), cross sections along the *XY* plane at various depths of the LLZO structures were examined. Since the thicknesses of Sample 1 (502 μm) and Sample 2 (545 μm) are similar, the selected cross sections are from the same position relative to the bottom of each film, i.e., 50, 350, and 500 μm from the bottom. The two-dimensional (2D) cross sections of the pores in each figure were identified and colored to distinguish them from the surrounding ones, as depicted in Figure 5a,b. The pores in almost all of the cross-sectional figures appear to have an elongated shape, except for the ones at the bottom of Sample 2, where more or less in-plane isotropic morphology was obtained. In both specimens, the pore sizes near the bottom where the slurries contacted the cooling plate are smaller than the ones in the middle and upper parts of the films. This gradient occurs because ice nucleates from the bottom, where the slurry is in direct contact with the freezing bed, and grows vertically along the thermal gradient.

To quantify the evolution of the pore size and shape, *XY* cross-sectional planes were extracted from bottom to top in 1 μm incremental steps for both samples, and at each thickness position, the pores were fitted with ellipses. The incremental step size was chosen based on the SR-μCT spatial resolution. After measuring the lengths of the long and short axes, designated *a* and *b*, respectively, of each ellipse, they were averaged at each thickness position and plotted in Figure 6a,b for Sample 1 and Sample 2. The lengths of *a* and *b* are smaller at the bottom, increasing gradually until they reach relatively constant values at about 80 μm from the bottom. After that point, the average lengths of both axes remain constant over a depth range of 300 μm. The pores in Sample 1 are larger on average than the ones in Sample 2. The pore sizes in the upper part near the surface of Sample 1 show little variation, while in the counterpart region in Sample 2, there is a significant decrease of *a*. The standard deviations of both axes are small at the very bottom of both films but increase rapidly and continuously toward the surface. The aspect ratios *a*/*b* averaged over each plane, plotted in Figure 6c,d, respectively, indicate that the pores are more stretched in the upper region than at the bottom for both samples. In general, the aspect ratios in Sample 1 are slightly greater and more consistently distributed through the thickness than those in Sample 2.

The equivalent diameter of each pore, ($d = \sqrt{a \times b}$), was calculated over an area of 0.4 mm^2 (500 × 800 μm^2) on the *XY* plane at four thickness positions: 50, 200, 350, and 500 μm from the bottom of both samples and the distributions are plotted (Figure 7). Most values of *d* are smaller than 40 μm near the bottom of both samples. This trend is maintained for all of the cross-sectional planes in Sample 2, although the fraction of large pores increases slightly in the regions farther from the bottom. In contrast, the number of pores with *d* larger than 40 μm increases in a much more significant manner in Sample 1, resulting in larger average pore sizes and fewer numbers of pores, as seen in Figure 7a. The number of pores increases slightly again in the regions closer to the surface, because more small-sized pores are formed. This may be due to surface water evaporation during freeze tape casting, leading to locally higher solid loading. To better describe the pore size distribution, the pores are sorted based on their equivalent diameters from small to large. Then, the area of the pores is added up one by one following the as-sorted sequence until the summation of the area reaches half of the total area, and this last-counted pore size is defined as the weighted median equivalent diameter. The weighted median equivalent diameters of the pores on each *XY* plane are plotted in Figure 7c. The weighted median equivalent diameter of the pores in Sample 1 increases from about 50−80 μm from the bottom to the surface, while that in Sample 2 first increases from 30 μm (bottom) to 50 μm (about 200 μm above the bottom) and then remains constant and decreases slightly toward the surface. Combining Figure 7a and c, it can be concluded that in the middle region of Sample 1, more large pores are generated but fewer small ones are left. Upon reaching the surface, the

DOI: 10.1021/acsami.9b11780
ACS Appl. Mater. Interfaces 2020, 12, 3494−3501

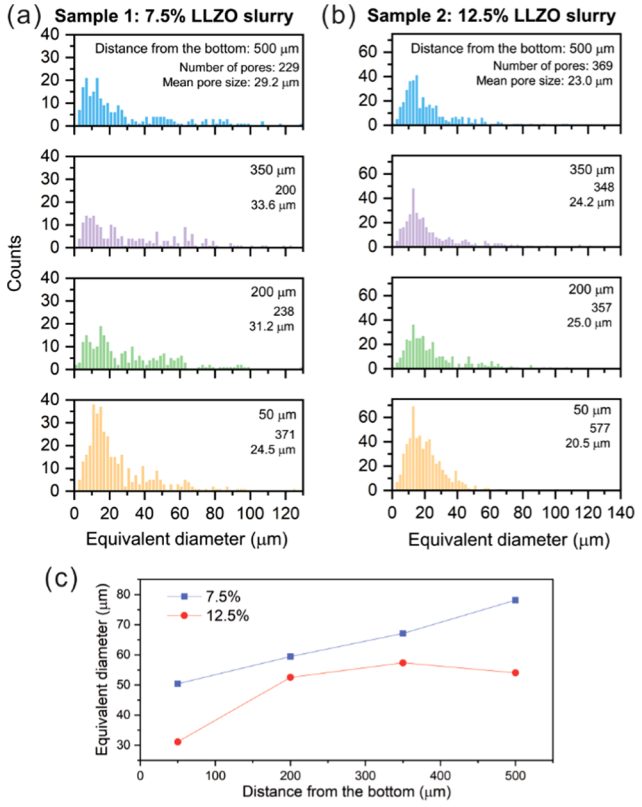

Figure 7. Pore size distribution for 7.5% (a) and 12.5% (b) samples at various thickness positions. The distance from the bottom, pore number, and mean pore size is labeled in each histogram. The weighted median equivalent diameters are calculated and displayed in (c).

total number and the equivalent diameter of pores go up simultaneously, indicating a wider distribution of pore sizes.

Based on the SR-μCT characterization and analysis displayed above, it is clear that freeze tape casting is a promising method for fabricating porous LLZO structures with directional open pore channels. The advantages are apparent in the following three aspects. First of all, high porosities of 75% or more can be readily obtained over a range of LLZO slurry concentrations using this technique. This is important for energy density reasons; active material loadings in the composite electrode should be high. Second, the pores are well aligned and have low tortuosity, which should enable facile infiltration of active materials, when fabricating composite cathodes. For 2D structures, the simplest mathematical method to estimate tortuosity (τ) is the arc-chord ratio, i.e., the ratio of the length of the curve (C) to the distance between the ends of it (L) $\tau = C/L$. Adapting this definition to our 3D model, the low tortuosity, approaching 1, also minimizes the Li^+ diffusional path length, which is critical for achieving good rate capability in operating electrochemical cells. Third, the pores, although they vary somewhat in size and morphology throughout the thicknesses of the samples, appear to have few bridges, which would interfere with efficient infiltration. Other advantages to the FTC process include scalability and environment friendliness when water is used as the solvent.

The evidence for graded porosity in the samples discussed above is of interest and requires some explanation. When the slurry is poured into the reservoir and carried out by the conveyor onto the freezing bed, the temperature at the bottom of the slurry is the lowest and thus the nucleation starts there. In the cases presented here, because the slurry was cooled well below its equilibrium freezing temperature, many solvent nuclei formed rapidly, having relatively small sizes and almost isotropic shapes. As a temperature gradient exists from the bottom (cold) to the surface (warm), the solvent crystals grow upwards along the temperature gradient direction. In doing so, the crystals coarsen by means of coalescing with one another and/or ripening. The cross-sectional morphology of the crystals deviates gradually from isotropy because another temperature gradient exists due to the movement of the conveyor, which is also the reason why the pores grow obliquely, not perpendicular to the LLZO film surface. Alignment can be made vertical by controlling the casting speed but this was not further investigated in this study. The pores in Sample 2 are smaller than those in Sample 1 because the solid loading in the slurry was higher. More bridges are also observed in Sample 2 than in Sample 1, probably due to two mechanisms. First, during the solidification, the solute solid in Sample 2 is higher than in Sample 1 and can go into the regions between adjacent solvent crystals and even, to some extent, impede the growth of the solvent crystal along the temperature gradient. Second, the lower solvent content of Sample 2 results in higher viscosity and lower diffusivity. As a result, it is easier for the solute to form connecting bridges. As the columnar crystals grow further up closer to the surface, the pore size and shape, especially in Sample 2, become more irregular, most likely caused by the change of local temperature and chemical composition. The larger average pore sizes, fewer bridges, and somewhat greater porosity of Sample 1, made with 7.5% LLZO, are more conducive to successful fabrication and utilization of composite electrodes for solid-state batteries than those of Sample 2, made with 12.5% LLZO.

To confirm the superior transport properties of the 3D LLZO scaffolds, ionic conductivities of a PEO/LiTFSI polymer electrolyte, LLZO powder/polymer composite electrolyte, and LLZO scaffold/polymer composite electrolyte were compared. The LLZO mass fraction in the composite electrolytes (65 wt % or 30 vol %) was fixed to identify the effect of LLZO distribution within the polymer matrix (homogeneous/discontinuous vs directional/continuous). Typical Nyquist plots of each sample are shown in Figure 8. Conductivities of the neat polymer electrolyte, LLZO powder/polymer composite electrolyte, and LLZO scaffold/polymer composite electrolyte are 3.6×10^{-6}, 5.3×10^{-6}, and 2.0×10^{-5} S/cm at room temperature, respectively. Both composite electrolytes show higher ionic conductivities compared to the neat polymer electrolyte. The composite using the LLZO scaffold has 4 times higher conductivity compared to the counterpart using LLZO powder and 6 times higher compared to the neat polymer electrolyte. A similar LLZO−PEO polymer composite electrolyte architecture has been reported recently using wood as the architectural template for constructing vertical LLZO channels.[33] A high ionic conductivity of 1.8×10^{-4} S/cm was obtained in their study but a much higher LLZO vol fraction (68%) was used in the composite compared to what is used here.

CONCLUSIONS

In this study, a freeze-tape-casting method was used to fabricate porous LLZO scaffolds for potential use in composite cathodes for solid-state batteries. The structures of two of

DOI: 10.1021/acsami.9b11780
ACS Appl. Mater. Interfaces 2020, 12, 3494−3501

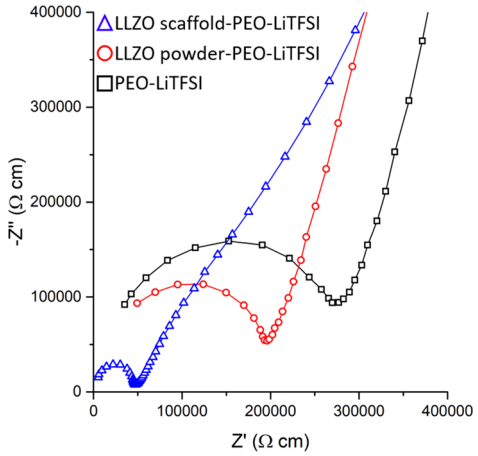

Figure 8. Nyquist plots of neat polymer electrolyte (PEO/LiTFSI), polymer electrolyte composited with LLZO particles, and LLZO scaffold infiltrated with PEO/LiTSI.

these LLZO scaffolds made using slurries with different solid loadings were characterized in detail with SR-μCT. A solid loading of 17.5% did not yield the desired structure, but scaffolds made from slurries containing 7.5 or 12.5% LLZO exhibited a unidirectional porosity of 75% or greater. The sample made with lower solid loading had somewhat higher porosity, larger pores on average, and less bridging between neighboring LLZO columns, which should be beneficial for the infiltration of active materials to make composite electrodes for solid-state batteries. In general, the wall thicknesses of the pores in the LLZO scaffolds show little change along the whole thickness range, in contrast to other material systems reported in previous freeze-tape-casting studies. Both samples exhibited a somewhat graded pore structure such that the pores were smaller close to the bottom (near the freezing bed) and somewhat larger close to the top. In addition, the pores were oriented at an oblique angle rather than perpendicular to the thickness of the samples. Both phenomena can be explained by the FTC fabrication process, in which a thermal gradient exists not only from the bottom to the top but also along the direction that the slurry is carried over the freezing bed. A scaffold infiltrated with a polymer electrolyte demonstrated higher room-temperature conductivity than either a polymer electrolyte alone or a polymer electrolyte containing LLZO, demonstrating the advantage of unidirectional pores.

■ ASSOCIATED CONTENT

Supporting Information

The Supporting Information is available free of charge at https://pubs.acs.org/doi/10.1021/acsami.9b11780.

Additional details including ellipse fitting for large area, reconstructed structure of the whole 17.5% sample, and reconstructed subvolume of 7.5% and 12.5% samples taken out along the X−Z and Y−Z planes (PDF)

Movies for displaying structures with 7.5, 12.5, and 17.5% LLZO loadings (AVI)

Movies for displaying structures with 7.5, 12.5, and 17.5% LLZO loadings (AVI)

Movies for displaying structures with 7.5, 12.5, and 17.5% LLZO loadings (AVI)

■ AUTHOR INFORMATION

Corresponding Authors

*E-mail: kchenlbl@gmail.com (K.C.).
*E-mail: mmdoeff@lbl.gov (M.M.D).

ORCID

Hao Shen: 0000-0002-1464-2608
Eongyu Yi: 0000-0002-6079-9382
Dilworth Y. Parkinson: 0000-0002-1817-0716
Guoying Chen: 0000-0002-3218-2609
Marca M. Doeff: 0000-0002-2148-8047

Notes

The authors declare no competing financial interest.

■ ACKNOWLEDGMENTS

This work is supported by the National Natural Science Foundation of China (Grant Nos. 51671154 and 91860109), the National Key Research and Development Program of China (Grant No. 2016YFB0700404), and the Assistant Secretary for Energy Efficiency and Renewable Energy, Office of Vehicle Technologies of the U.S. Department of Energy under Contract No. DE-AC02-05CH11231. This research uses resources of the Advanced Light Source, which is a DOE Office of Science User Facility under contract no. DE-AC02-05CH11231. H.S. would like to thank the financial support from the program of China Scholarship Council (No. 201606280062) from Oct 2016 to Sep. 2017 and from ALS Doctoral Fellowship in Residence from Oct 2017 to Sep. 2018. K.C. appreciates the support from the International Joint Laboratory for Micro/Nano Manufacturing and Measurement Technologies and the Collaborative Innovation Center of High-End Manufacturing Equipment. This document was prepared as an account of work sponsored by the United States Government. While this document is believed to contain correct information, neither the United States Government nor any agency thereof, nor the Regents of the University of California, nor any of their employees, makes any warranty, express or implied, or assumes any legal responsibility for the accuracy, completeness, or usefulness of any information, apparatus, product, or process disclosed, or represents that its use would not infringe privately owned rights. Reference herein to any specific commercial product, process, or service by its trade name, trademark, manufacturer, or otherwise does not necessarily constitute or imply its endorsement, recommendation, or favoring by the United States Government or any agency thereof, or the Regents of the University of California. The views and opinions of the authors expressed herein do not necessarily state or reflect those of the United States Government or any agency thereof or the Regents of the University of California.

■ REFERENCES

(1) Lin, D.; Liu, Y.; Cui, Y. Reviving the Lithium Metal Anode for High-energy Batteries. *Nat. Nanotechnol.* **2017**, *12*, 194−206.
(2) Deng, D. Li-Ion Batteries: Basics, Progress, and Challenges. *Energy Sci. Eng.* **2015**, *3*, 385−418.
(3) Porz, L.; Swamy, T.; Sheldon, B. W.; Rettenwander, D.; Frömling, T.; Thaman, H. L.; Berendts, S.; Uecker, R.; Carter, W. C.; Chiang, Y.-M. Mechanism of Lithium Metal Penetration through Inorganic Solid Electrolytes. *Adv. Energy Mater.* **2017**, *7*, No. 1701003.
(4) Bai, P.; Li, J.; Brushett, F. R.; Bazant, M. Z. Transition of Lithium Growth Mechanisms in Liquid Electrolytes. *Energy Environ. Sci.* **2016**, *9*, 3221−3229.

DOI: 10.1021/acsami.9b11780
ACS Appl. Mater. Interfaces 2020, 12, 3494−3501

(5) Zhang, Z.; Shao, Y.; Lotsch, B. V.; Hu, Y.-S.; Li, H.; Janek, J.; Nan, C.; Nazar, L.; Maier, J.; Armand, M.; Chen, L. New Horizons for Inorganic Solid State Ion Conductors. *Energy Environ. Sci.* **2018**, *11*, 1945−1976.
(6) Gambe, Y.; Sun, Y.; Honma, I. Development of Bipolar All-solid-state Lithium Battery Based on Quasi-solid-state Electrolyte Containing Tetraglyme-LiTFSA Equimolar Complex. *Sci. Rep.* **2015**, *5*, No. 8869.
(7) Yu, S.; Schmidt, R. D.; Garcia-Mendez, R.; Herbert, E.; Dudney, N. J.; Wolfenstine, J. B.; Sakamoto, J.; Siegel, D. J. Elastic Properties of the Solid Electrolyte $Li_7La_3Zr_2O_{12}$ (LLZO). *Chem. Mater.* **2016**, *28*, 197−206.
(8) Han, F.; Zhu, Y.; He, X.; Mo, Y.; Wang, C. Electrochemical Stability of $Li_{10}GeP_2S_{12}$ and $Li_7La_3Zr_2O_{12}$ Solid Electrolytes. *Adv. Energy Mater.* **2016**, *6*, No. 1501590.
(9) Kotobuki, M.; Munakata, H.; Kanamura, K.; Sato, Y.; Yoshida, T. Compatibility of $Li_7La_3Zr_2O_{12}$ Solid Electrolyte to All-Solid-State Battery Using Li Metal Anode. *J. Electrochem. Soc.* **2010**, *157*, A1076−A1079.
(10) Ni, J. E.; Case, E. D.; Sakamoto, J. S.; Rangasamy, E.; Wolfenstine, J. B. Room Temperature Elastic Moduli and Vickers Hardness of Hot-Pressed LLZO Cubic Garnet. *J. Mater. Sci.* **2012**, *47*, 7978−7985.
(11) Ohta, S.; Kobayashi, T.; Seki, J.; Asaoka, T. Electrochemical Performance of an All-Solid-State Lithium Ion Battery with Garnet-Type Oxide Electrolyte. *J. Power Sources* **2012**, *202*, 332−335.
(12) Shen, H.; Yi, E.; Cheng, L.; Amores, M.; Chen, G.; Sofie, S. W.; Doeff, M. M. Solid-State Electrolyte Considerations for Electric Vehicle Batteries. *Sustainable Energy Fuels* **2019**, *3*, 1647−1659.
(13) Han, X.; Gong, Y.; Fu, K.; He, X.; Hitz, G. T.; Dai, J.; Pearse, A.; Liu, B.; Wang, H.; Rubloff, G.; Mo, Y.; Thangadurai, V.; Wachsman, E. D.; Hu, L. Negating Interfacial Impedance in Garnet-Based Solid-State Li Metal Batteries. *Nat. Mater.* **2017**, *16*, 572.
(14) Cheng, L.; Park, J. S.; Hou, H.; Zorba, V.; Chen, G.; Richardson, T.; Cabana, J.; Russo, R.; Doeff, M. Effect of Microstructure and Surface Impurity Segregation on the Electrical and Electrochemical Properties of Dense Al-Substituted $Li_7La_3Zr_2O_{12}$. *J. Mater. Chem. A* **2014**, *2*, 172−181.
(15) Sharafi, A.; Meyer, H. M.; Nanda, J.; Wolfenstine, J.; Sakamoto, J. Characterizing the Li−$Li_7La_3Zr_2O_{12}$ Interface Stability and Kinetics as a Function of Temperature and Current Density. *J. Power Sources* **2016**, *302*, 135−139.
(16) Tsai, C. L.; Roddatis, V.; Chandran, C. V.; Ma, Q.; Uhlenbruck, S.; Bram, M.; Heitjans, P.; Guillon, O. $Li_7La_3Zr_2O_{12}$ Interface Modification for Li Dendrite Prevention. *ACS Appl. Mater. Interfaces* **2016**, *8*, 10617−10626.
(17) Fu, K.; Gong, Y.; Hitz, G. T.; McOwen, D. W.; Li, Y.; Xu, S.; Wen, Y.; Zhang, L.; Wang, C.; Pastel, G.; Dai, J.; Liu, B.; Xie, H.; Yao, Y.; Wachsman, E. D.; Hu, L. Three-Dimensional Bilayer Garnet Solid Electrolyte Based High Energy Density Lithium Metal−Sulfur Batteries. *Energy Environ. Sci.* **2017**, *10*, 1568−1575.
(18) McOwen, D. W.; Xu, S.; Gong, Y.; Wen, Y.; Godbey, G. L.; Gritton, J. E.; Hamann, T. R.; Dai, J.; Hitz, G. T.; Hu, L.; Wachsman, E. D. 3D-Printing Electrolytes for Solid-State Batteries. *Adv. Mater.* **2018**, *30*, No. e1707132.
(19) Chen, Y.; Bunch, J.; Li, T.; Mao, Z.; Chen, F. Novel Functionally Graded Acicular Electrode for Solid Oxide Cells Fabricated by the Freeze-Tape-Casting Process. *J. Power Sources* **2012**, *213*, 93−99.
(20) Gannon, P.; Sofie, S.; Deibert, M.; Smith, R.; Gorokhovsky, V. Thin Film YSZ Coatings on Functionally Graded Freeze Cast NiO/YSZ SOFC Anode Supports. *J. Appl. Electrochem.* **2009**, *39*, 497−502.
(21) Sofie, S. W. Fabrication of Functionally Graded and Aligned Porosity in Thin Ceramic Substrates with the Novel Freeze-Tape-Casting Process. *J. Am. Ceram. Soc.* **2007**, *90*, 2024−2031.
(22) Liu, X.; Rahaman, M. N.; Fu, Q. Oriented Bioactive Glass (13-93) Scaffolds with Controllable Pore Size by Unidirectional Freezing of Camphene-Based Suspensions: Microstructure and Mechanical Response. *Acta Biomater.* **2011**, *7*, 406−416.
(23) Cheng, L.; Crumlin, E. J.; Chen, W.; Qiao, R.; Hou, H.; Franz Lux, S.; Zorba, V.; Russo, R.; Kostecki, R.; Liu, Z.; Persson, K.; Yang, W.; Cabana, J.; Richardson, T.; Chen, G.; Doeff, M. The Origin of High Electrolyte-Electrode Interfacial Resistances in Lithium Cells Containing Garnet Type Solid Electrolytes. *Phys. Chem. Chem. Phys.* **2014**, *16*, 18294−18300.
(24) Xia, W.; Xu, B.; Duan, H.; Tang, X.; Guo, Y.; Kang, H.; Li, H.; Liu, H. Reaction Mechanisms of Lithium Garnet Pellets in Ambient Air: The Effect of Humidity and CO_2. *J. Am. Ceram. Soc.* **2017**, *100*, 2832−2839.
(25) Shen, H.; Yi, E.; Amores, M.; Cheng, L.; Tamura, N.; Parkinson, D. Y.; Chen, G.; Chen, K.; Doeff, M. Oriented Porous LLZO 3D Structures Obtained by Freeze Casting for Battery Applications. *J. Mater. Chem. A* **2019**, *7*, 20861−20870.
(26) Cheng, L.; Liu, M.; Mehta, A.; Xin, H.; Lin, F.; Persson, K.; Chen, G.; Crumlin, E.; Doeff, M. Garnet Electrolyte Surface Degradation and Recovery. *ACS Applied Energy Materials* **2018**, *1*, 7244−7252.
(27) Gürsoy, D.; De Carlo, F.; Xiao, X.; Jacobsen, C. TomoPy: A Framework for the Analysis of Synchrotron Tomographic Data. *J. Synchrotron Radiat.* **2014**, *21*, 1188−1193.
(28) Pandolfi, R. J.; Allan, D. B.; Arenholz, E.; Barroso-Luque, L.; Campbell, S. I.; Caswell, T. A.; Blair, A.; De Carlo, F.; Fackler, S.; Fournier, A. P.; Freychet, G.; Fukuto, M.; Gürsoy, Da.; Jiang, Z.; Krishnan, H.; Kumar, D.; Kline, R. J.; Li, R.; Liman, C.; Marchesini, S.; Mehta, A.; N'Diaye, A. T.; Parkinson, D. Y.; Parks, H.; Pellouchoud, L. A.; Perciano, T.; Ren, F.; Sahoo, S.; Strzalka, J.; Sunday, D.; Tassone, C. J.; Ushizima, D.; Venkatakrishnan, S.; Yager, K. G.; Zwart, P.; Sethian, J. A.; Hexemer, A. Xi-Cam: A Versatile Interface for Data Visualization and Analysis. *J. Synchrotron Radiat.* **2018**, *25*, 1261−1270.
(29) Schneider, C. A.; Rasband, W. S.; Eliceiri, K. W. NIH Image to ImageJ: 25 Years of Image Analysis. *Nat. Methods* **2012**, *9*, 671−675.
(30) Brocher, J. *The BioVoxxel Image Processing and Analysis Toolbox*, EuBIAS-Conference, Paris, France; Jan 5-6, 2015.
(31) Wagner, T.; Eglinger, J. *Thorstenwagner/ij-ellipsesplit: EllipseSplit 0.6.0 SNAPSHOT*.Zenodo, 2017.
(32) Deville, S. Freeze-Casting of Porous Ceramics: A Review of Current Achievements and Issues. *Adv. Eng. Mater.* **2008**, *10*, 155−169.
(33) Dai, J.; Fu, K.; Gong, Y.; Song, J.; Chen, C.; Yao, Y.; Pastel, G.; Zhang, L.; Wachsman, E.; Hu, L. Flexible Solid-State Electrolyte with Aligned Nanostructures Derived from Wood. *ACS Mater. Lett.* **2019**, *1*, 354−361.

DOI: 10.1021/acsami.9b11780
ACS Appl. Mater. Interfaces 2020, 12, 3494−3501